Shape Change Propagation Through Soft Curved Materials for Dynamically-Tuned Paddling Robots

Yuhao Jiang¹, Mohammad Sharifzadeh², Daniel M. Aukes^{2*}

Abstract—This paper introduces a method of transmitting actuation forces through soft, curved materials for use in swimming applications. This concept leverages the mechanics of materials to generate highly nonlinear stiffness and buckling behavior that induces an asymmetric paddling gait in the endeffector, a locomotion strategy seen throughout biology. This approach can be used to simplify actuation signals in soft robotic systems. A soft tubular swimming device has thus been developed which utilizes the proposed shape propagation concept; it is actuated by a soft pneumatic actuator which has been adapted to be co-printed within the tubular geometry and change the tube's curvature when inflated. This work is validated experimentally as well as through the use of FEA and dynamic models, which tell us how altering various design geometry and dynamic parameters can play a role in generating non-zero forward thrust and positive work on the environment. The final, 40 mm long prototype reaches 53 mm/s, 1.33 body lengths per second, when swimming underwater.

I. INTRODUCTION

While the field of soft robotics has led to a number of recent innovations in tuned-stiffness materials, less work has been done on the role curvature can play in tuning locomotion dynamics in soft systems. This paper investigates a concept of using connected, curved, soft surfaces to transmit actuation effort and tune the directional stiffness of appendages in underwater swimming. This shape propagation concept leverages the mechanics of materials and studies the impact that curvature can have on the ability to transmit shape change between two different surfaces of a soft body in order to simplify the power delivery and control signals required for locomoting soft robotic systems. This has led to the development of a soft tubular device that adopts the proposed shape propagation concept that can generate forward net thrust and positive work on the underwater environment over a gait cycle. As seen in Fig. 1, the proposed device transmits the deformation of a central tube to two connected curved fins to produce an asymmetric paddling stroke in which the anisotropic stiffness of curved surfaces is leveraged to preferentially buckle the system in one direction. Furthermore, this device can be 3D printed in a single step without any assembly, through its integration of a revised pneu-nets pneumatic actuator.

This material is based upon work supported by the National Science Foundation under Grant No. 1935324.

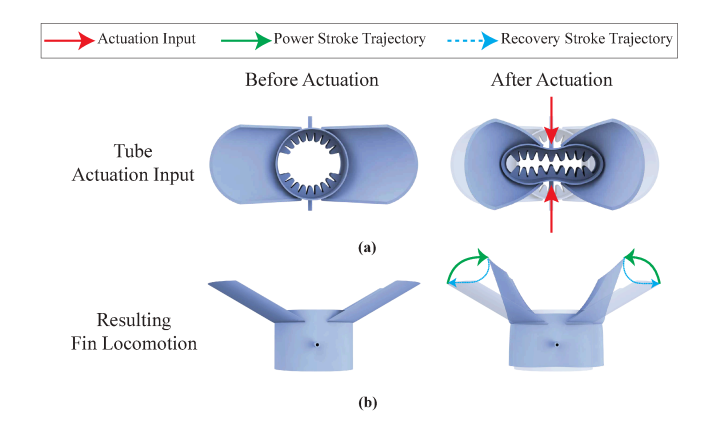


Fig. 1. Conceptual rendering (a): Conceptual rendering of the tube actuation input. (b): Conceptual rendering of the resulting locomotion on the side fins.

Paddling is a locomotion strategy commonly found in organisms such as the backswimmer [1], frog [2]-[4], turtle [5], [6], fruit fly [7] and dog [8]. A number of studies have shed light on the use of paddling in human activities such as the breaststroke [9]-[12] and canoeing [13]. In these examples, the leg, appendage, wing, or paddle moves through an asymmetric motion that generates positive average forward thrust and positive work on its surroundings. Robotic systems have also been developed that replicate paddling gaits, such as [14]–[20]. However, these approaches typically rely on asymmetric actuation, requiring higher degree-offreedom designs with carefully-optimized input signals to form the desired gait. This can impact resulting systems by increasing complexity, reducing reliability - especially in underwater applications – and ultimately driving up the cost of the robot. In contrast to this surveyed prior work, we seek in this paper to produce positive forward thrust using an asymmetric paddling gait via one symmetric actuation input. This is realized by tuning the stiffness of our system fin to alter the fin critical buckling limit during the paddling cycle.

To alter the curvature of thin sheet structures, a technique called curved crease folding has been well studied and used within origami, the art of paper folding. Curved crease folding uses the principle of a curved paper crease to establish and propagate curvature across two connected developable surfaces. This principle has been studied computationally [21]–[25] as well as applied to the field of graphics [26], [27], architecture [27], and robotics [28]. Curved crease folding traditionally observes a number of rules that help simplify the analysis of how curvature-based relationships are established, including the assumption of rigid and inextensible paper sheets that are infinitely thin. Combined with the assumption

¹School for Engineering of Matter, Transport and Energy, Fulton Schools of Engineering, Arizona State University, Tempe, AZ, 85281, USA yuhao92@asu.edu

²The Polytechnic School, Fulton Schools of Engineering, Arizona State University, Mesa, AZ, 85212, USA

^{*}Address all correspondence to this author. danaukes@asu.edu

of flat-foldability, this assumes that gaussian curvature of curved-crease geometries must remain zero. Although curved crease folding shares some common features with the concept proposed in this paper, these basic assumptions do not hold for several reasons. First, we use soft material that is extensible in all dimensions. Second, the geometries utilized in this paper cannot be considered to be infinitely thin, and plays a role in the development and transmission of curvature. And finally our selected manufacturing method of 3D printing permits the generation of surfaces with both positive and negative Gaussian curvature. Nevertheless, the principle of curved-crease folding, and the rules which govern the transfer of curvature between surfaces, is a significant source of inspiration in this work.

Prior work has established that directional stiffness of a thin curved sheet can be changed by tuning its curvature [29]. This concept has been extended to soft tubular structures, in which the stiffness can be tuned by altering the tube's curvature; this has been validated using FEA and experimental approaches [30]. The mechanics of buckling and "snap-through" in curved shells has also been studied [31]. Buckling, as a principal mechanism, has been found to effectively generate locomotions in flagella [32], Venus flytraps [33], [34], and ladybird beetles [35].

Tunable stiffness permits the occurrence of anisotropic buckling, which eventually results in an asymmetric paddling gait, which has also been studied in our previous work [36], in which a new concept to generate forward thrust was proposed; by taking advantage of the nature of curved beams to preferentially buckle under loads, this concept demonstrates how, using symmetric actuation signals, the complexity of input signals can be reduced in comparison to alternative robotic paddling swimmer designs. In this paper, we have adapted the same concept to simplify actuation complexity. Like the previous work, the fin used in this paper is pre-curved so that it possesses similar asymmetric stiffness and critical buckling limits; this creates a controllable, hysteretic paddling gait under certain symmetric actuator signals. Differing from the previous work where the curved beam is rigidly attached to an actuator and establishing a 1:1 relationship between a motor and its output, in this work, we are interested in utilizing the curvature change as a source of the actuation to permit the actuation transmission from pinching the tube to the paddling of the fin.

The contributions of this paper are: (i) Developing a 3D printable soft tubular swimming device that utilizes the concept of curvature propagation and anisotropic buckling to produce an asymmetric paddling gait via a symmetric actuating input. (ii) Establishing a dynamic model for the proposed device to reveal the role inertia and drag play on anisotropic buckling, hysteresis behavior, and asymmetric paddling gait. (iii) Showing how a 3D printable pneu-nets based actuator can be adapted to pinch the tube.

The rest of the paper is organized as follows: in Section II, we introduce three assumptions to better understand the operational concept of shape propagation; in Section III, we validate the first assumption by developing a pneumatic

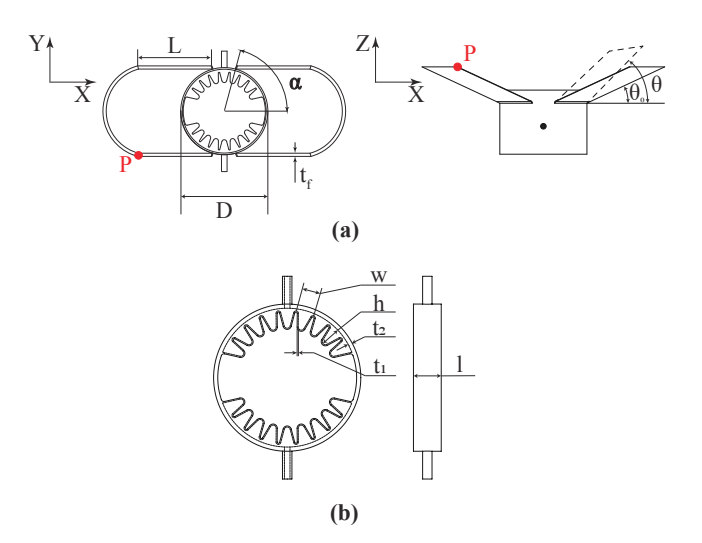


Fig. 2. **Design variables (a):** Design variables of the swimming device. **(b):** Design Variables of the pneumatic actuator.

actuator to demonstrate curvature change of the tube via pinching; in Section IV, we discuss the relationship between the tube's curvature change and fin locomotion; in section V, we study the relationship between fin curvature and buckling limit; we then study the swimming capability of a proposed device. This is aided by a dynamic model that considers anisotropic buckling behavior due to stiffness changes that lead to asymmetric paddling gaits. We conclude the paper with a discussion of improvements that can be made to our current design, and future work to apply this concept to swimming robots.

II. CONCEPT OF OPERATION

In this section, we introduce the operational concept of the proposed device. This idea is based upon three main assumptions. The first assumption is that pneumatic, bellowsstyle actuators mounted on the inside of a tube may be used to pinch and deform a tube radially, as illustrated by the red arrows in Fig. 1a. The second states that curvature changes due to the tube's deformation may be transmitted via the principles of continuum mechanics to distally-attached curved surfaces such as the attached fins seen in Fig. 1b, causing these surfaces to be swept inward closer to the tube while changing curvature in the process. The third assumption is that this sweeping motion and curvature change can be used to create paddling gaits, as indicated by the green and blue arrows in Fig. 1b. Asymmetric paddling is caused by the anisotropic buckling behavior of curved fins, which, as mentioned in the introduction, establishes a non-reciprocal motion trajectory for the fin that generates nonzero net thrust over a full gait cycle. This assumption is further supported by prior work on buckling curved beams [36], which we extend in this paper by demonstrating how tuning the drag and inertia of such systems can alter the hysteresis observed in order to perform positive net work in underwater locomotion applications.

This paper seeks to validate the aforementioned assumptions and demonstrate how, when connected together, the

effects of propogated curvature, nonlinear stiffness, and buckling can be tuned to establish and improve forward thrust and motion generation in this device. This is done in the design process by tuning several parameters, such as those seen in Fig. 2. Some parameters influence the overall stiffness of the tube-fin system, such as the tube wall thickness t_2 , the tube diameter D, the fin thickness t_f . Other parameters, such as the actuator wall thickness t_2 , the actuator chamber width w, the actuator chamber height h, and the actuator chamber length l, are responsible for establishing the force generation capabilities of the pneu-nets actuator. Other variables, such as the fin arc length (α) and the fin attachment angle (θ) define the geometric connection between the tube and fin and establish the travel and curvature-change relationships between the two surfaces. It should be noted that the initial radius of curvature of the tube and fin are set equal to each other in this study. Other variables seen within the plot in Fig. 2 assist in tracking and measuring displacement and deformation. These include the point P, whose motion along different axes can be used to describe the change in curvature as well as the total travel of the fin. We thus introduce y, which tracks the displacement of P along the Y-axis; this value increases as the curvature of the fin increases. The travel of point P in the X-Z plane is measured by s; the higher the value of s, the greater the travel from P's neutral position, indicating a higher range of motion.

III. VALIDATING ASSUMPTION I: PNEUMATIC TUBE PINCHING ACTUATOR

The first assumption is validated in this section through the development of a bellows-style pneumatic actuator that can be mounted inside a soft tube to flatten it along a desired axis. In previous work [30], a tendon-based, servo-driven actuation system was developed to pinch and radially deform a soft tube in multiple directions. That approach, requiring rigid exterior cable routing through pulleys mounted to the ground, proved both complex and impractical given our desire to migrate toward untethered, underwater applications. Thus in this paper we have adapted a pneumatic actuator design inspired by the class of commonly-used pneumatic elastomeric actuators called pneu-nets [37] so that it can be co-printed within a soft tubular body. Pneu-nets actuators have been applied to a variety of soft robotic applications, due to their relatively compact size, flexibility, and good actuating power [38]; they have also been extensively modeled for the purposes of increasing performance across a number of criteria such as force, power, and displacement [39], [40]. Though early pneu-nets were cast in soft rubber, more recent designs have been subsequently adapted for 3D printing [39], [41]. In contrast to prior work - in which actuators are typically flat in their unactuated state and curve when actuated - we have adapted the geometry of our design so that it may be co-printed within a soft tube in order to flatten when inflated.

The process of developing the actuator starts by understanding how the parameters relating to device geometry (as seen in Fig. 2b) impact performance. The five key variables include the number of chambers on each side, n, chamber wall thickness (t_1) , height (h), width (w), and length (l). The thickness of the chamber wall (t_1) influences the ability of the actuator to retain pressure without leaking, and is influenced both by the material as well as the resolution of the 3D printer. A thinner chamber wall requires lower pressures to deform but results in leaking and poor seals due to the limitation of the 3D printing process. Thus, given the resolution of our 3D printer, t_1 was set at 0.4 mm. A number of different prototypes with variable number of chambers, chamber heights, and chamber widths were then prototyped and evaluated against each other. By inflating the prototypes to the same pressure and comparing the deformation of each, we reached the design parameters as shown in Table. I.

A variety of materials were considered for use in the actuator against a number of design constraints such as stiffness, compatibility with 3D printing, and impermeability with water and air. These constraints ultimately helped focus our search on a small set of materials. With regard to material stiffness, our goal was to select a material that reduced internal losses due to stretching, while being able to transmit curvature changes over longer distances. Compatibility with 3D printing was considered, not just with regard to temperature, extruder size, and other process characteristics, but with the quality of resulting small feature sizes - such as wall thickness - that impacted the ability of the resulting bladders to operate under high pressures without leaking or popping. Finally, actuator performance was ultimately evaluated by each actuator's respective ability to repeatedly and quickly deform the tube it was mounted within. Based on the above desired characteristics and constraints, two different materials were compared in-depth: thermoplastic polyurethane (TPU) with a shore hardness of 95A [42], and thermoplastic elastomer (TPE) with shore hardness of 92A [43]. To select the material that performed best against our various criteria, we printed two prototypes of the same geometry using both materials, as shown in Fig. 3a. In order to compare each material's impermeability to air and water, we compared the layer-to-layer bonding characteristics between the two materials. The quality of the bond between successive layers of TPE was observed to be both smoother and tighter than TPU, which may be attributed to the lower melting temperature of TPE (147 $^{\circ}C$) vs TPU (220 $^{\circ}C$). This can be seen in Fig. 3b; both prototypes were printed using the same design parameters and the manufacturer's recommended printing parameters. Hence, TPE was selected for the final device.

IV. VALIDATING ASSUMPTION II: CURVATURE PROPAGATION BETWEEN TUBE AND THE ATTACHED FINS

In this section, we validate the second assumption via FEA. The second assumption is difficult to study using first principle derivations and analytical expressions for a number of reasons. First, the geometries involved – three-dimensional surfaces and curved attachment geometries – are complex problems difficult to represent analytically, especially when working with soft or flexible materials in a fluid environment.

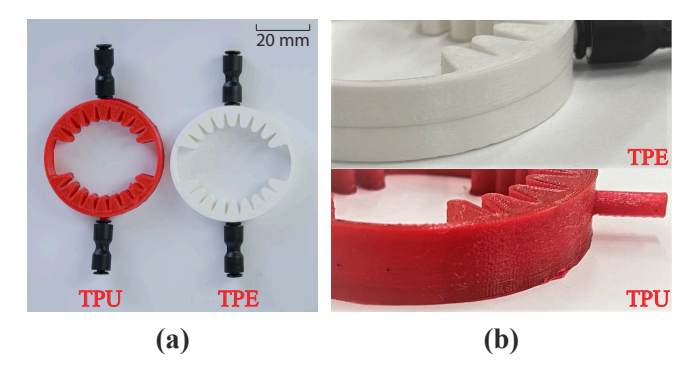


Fig. 3. Material Assessment. (a): The proposed actuator made of TPU and TPE. (b): Comparison of the layer bonding performance.

Thus we have taken the approach to use FEA to understand the impact of curvature and compliance on deformation in soft structures. For our use, FEA permits the modeling of soft continuum mechanics and thus benefits the study on validating the proposed assumption and exploring the relation between design variables and paddling gaits.

A. Concept Validation

To validate the concept that the tube's deformation can be propagated and transmitted to actuate the paddling gait of the fins as well as to alter fin curvature, we conducted a FEA simulation to analyze the fin displacement during the deformation of the tube. The FEA analysis was conducted in Ansys Mechanical ¹ using static structral analysis with force convergence criteria. The mesh size is 0.002 *m*, the number of meshing elements is 68578, the total analysis step is 200, and the analyzing time for each study takes around 25 min using a 24 thread computing workstation.

In order to develop a durable connection between the fin and the tube, the fin's radius of curvature in its neutral configuration is set to equal the radius of the tube. In the simulation, the tube is pinched along the Y-axis at the midpoint of the tube in 200, 0.165 mm increments until the Y-axis displacement reaches 33 mm, or 95% of the tube's deformation range; throughout this process the fins sweep inward and their curvature increases. The FEA result at the initial and the final step is shown in Fig. 4d and Fig. 4e, respectively. To measure this effect, the maximum planar Xaxis, Y-axis, and Z-axis displacement of the fin was analyzed by measuring the displacement of point P (shown in Fig. 2a). As shown in Fig. 4a, as the tube is increasingly pinched, the fin's displacement grows accordingly. The fin's planar travel, calculated by the total displacement in the X-Z plane, indicates the paddling stroke of the fin, while the Y-axis displacement represents the fin's curvature change during the deformation of the tube. This result validates the proposed concept that the deformation of the tube can be propagated to produce the fin paddling gait as well as to alter the curvature of the fin. The animation of this result is shown in the supplementary video.

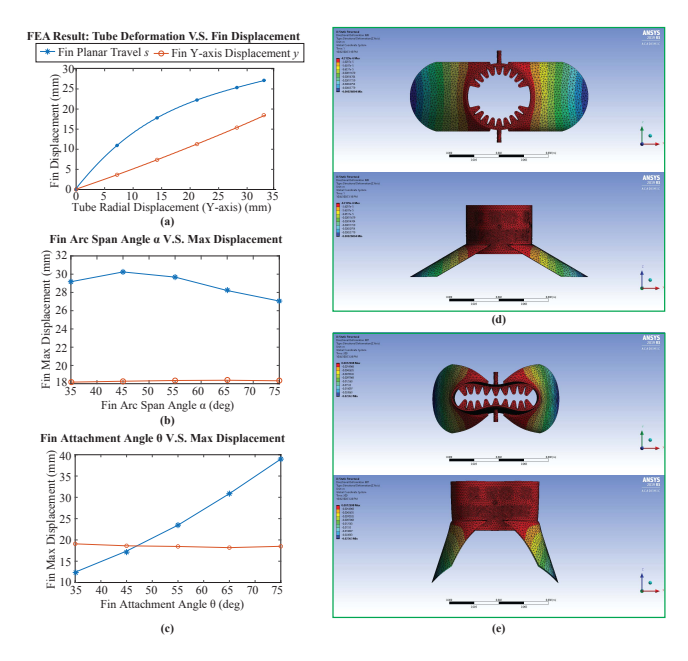


Fig. 4. **FEA Validation.** (a): Concept validation via FEA. (b): FEA result of the relation between the fin arc length angle and the fin max displacement along Y-axis and the fin's max travel. (c): FEA result of the relation between the fin attachment angle and the fin max displacement along Y-axis and the fin's max travel. (d): FEA result at initial step. (e): FEA result at final step.

B. Design Configuration VS Paddling Performance

In order to evaluate the design configuration and assess paddling performance, we seek to explore the relationship between α , θ , and the fin's maximum travel, s (as defined in Section IV). Determining the role these two variables play on s establishes the effective transmission ratio between the tube's deformation and the forces exerted at the fins, which can be useful for tuning the relative loading of the structures to induce buckling and hysterisis. Furthermore, we also study the role these two variables play in changing s, the curvature of the fin. Understanding how curvature change during the fin's sweep affects its nonlinear stiffness profile as well as its critical buckling limits in positive and negative bending are useful in design.

To understand the relationship between α , y, and s during the deformation of the tube, six simulations were conducted with different values of α for the same tube displacement (0-33 mm). Attachment angle θ is held constant at 75°; all other design parameters are shown in Table I. As can be seen in Fig. 4b, the impact of α on y and s is negligible.

The relationship between θ , y, and s was also studied across six designs where θ was varied between 35° - 75° . In this case α was held constant at 75° , while the remaining design parameters are shown in Table I. The results, shown in Fig. 4c, reveal a high correlation between attachment angle (θ) and travel (s) without a significant effect on curvature change (y). Based on these results as well as the size limitations of the 3D printer, we selected the design parameters for the final prototype, which are shown in Table I.

¹Ansys[®], Inc. Mechanical Products 2019 R3

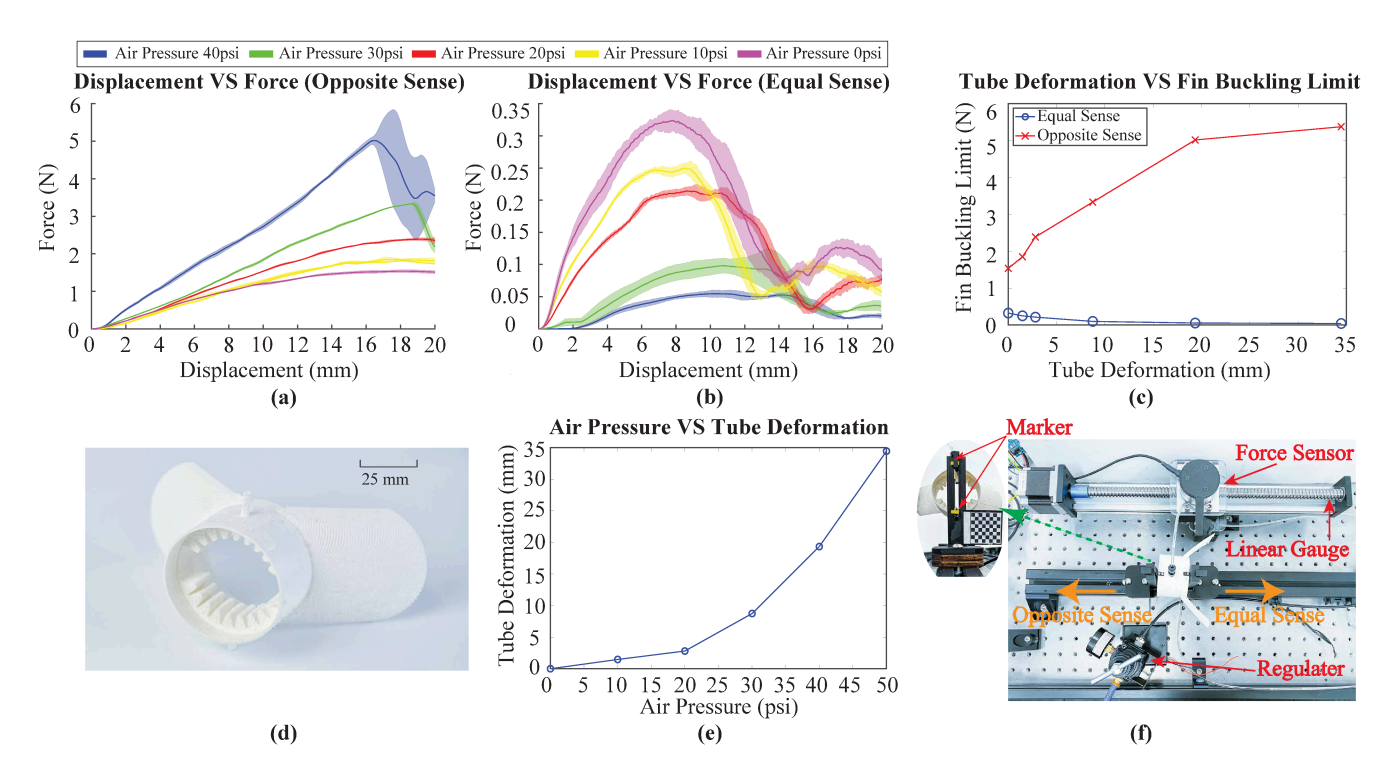


Fig. 5. **Fin Buckling Test.** (a): The fin drag force data collected when the pusher moves in opposite sense under different tube deformation states. (b): The fin drag force data collected when the pusher moves in equal sense under different tube deformation states. (c): The fin critical buckling limit in both opposite sense and equal sense under different tube deformation. (d): The final prototype. (e): The tube deformation under different inflation air pressure. (f): The test setup.

V. VALIDATING ASSUMPTION III: CURVATURE CHANGE IN FINS AND THE NONRECIPROCAL PADDLING

In this section, we validate the third assumption experimentally and with a derived dynamic model. The actuator described in Section III is embedded within a longer tube attached to two curved fins, as studied in the FEA model described in Section IV. The device is manufactured on an Ultimaker S5 Pro 3D printer using 3DXFlex TPE filament [43]. The final prototype is shown in Fig. 5d.

A. Evaluation of Fin Buckling Limits

As discussed previously, buckling of curved beams can be influenced by the propogation of curvature from the central tube when it is pinched. To generate positive forward thrust, the buckling limit supporting the drag forces experienced during the power stroke (opposite-sense) must to be higher than the buckling limit experienced by the drag forces during the recovery stroke (equal-sense), as indicated in Fig. 5f.

The fin's critical buckling limit was obtained with the prototype to validate this third assumption. As seen in the FEA test in Section IV-A, when the tube deforms, the curvature of the fin changes accordingly, resulting in a configuration-dependent fin buckling limit. In this test, the fin's buckling limit was thus obtained at different curvatures. The test setup can be seen in Fig. 5f. The main tube's deformation was controlled by regulating the air pressure into the actuator, deforming the tube incrementally at five pressure values from 0-40 psi until it reached its flat state. The tube's displacement can be measured by the position change of two markers attached to the fixture. The result shown in Fig. 5e shows

the relationship between inflation air pressure and the tube's deformation. At each pressure, a push plate driven on a linear rail pushed the fin over 20 mm in both directions from the fin's neutral configuration while the force was recorded. In order to receive a reliable static result, the test was conducted five times for each pressure configuration. The shaded error bar plots in Figs. 5a, b show the force data collected in the equal and opposite sense across for each pressure value. As can be seen in Fig. 5a, when the push plate moves in the opposite sense direction, representing the power stroke, the maximum force reaches 5.02 N. In contrast, as seen in the Fig. 5b, in the equal-sense direction (representing the recovery stroke), the maximum drag reaches only 0.32 N. To further highlight the asymmetric buckling limit on each side of the fin, the maximum drag experienced in both directions from Figs. 5a, b has been plotted in Fig. 5c. The difference in buckling limits between the two orientations of the fin demonstrates the anisotropic behavior made possible via the fin's curvature. The trend found in Fig. 5c indicates that, as the tube deforms, and the fin moves closer to the body, the increased curvature change raises the buckling limit in the opposite sense while weakening the buckling limit in the equal sense.

B. Swimming Thrust

Based upon the validity of the three assumptions above, the proposed device should be expected to be able to swim forward. In this section, we validate this hypothesis experimentally by measuring the thrust generated by the prototype as well as the maximum swimming speed. The net

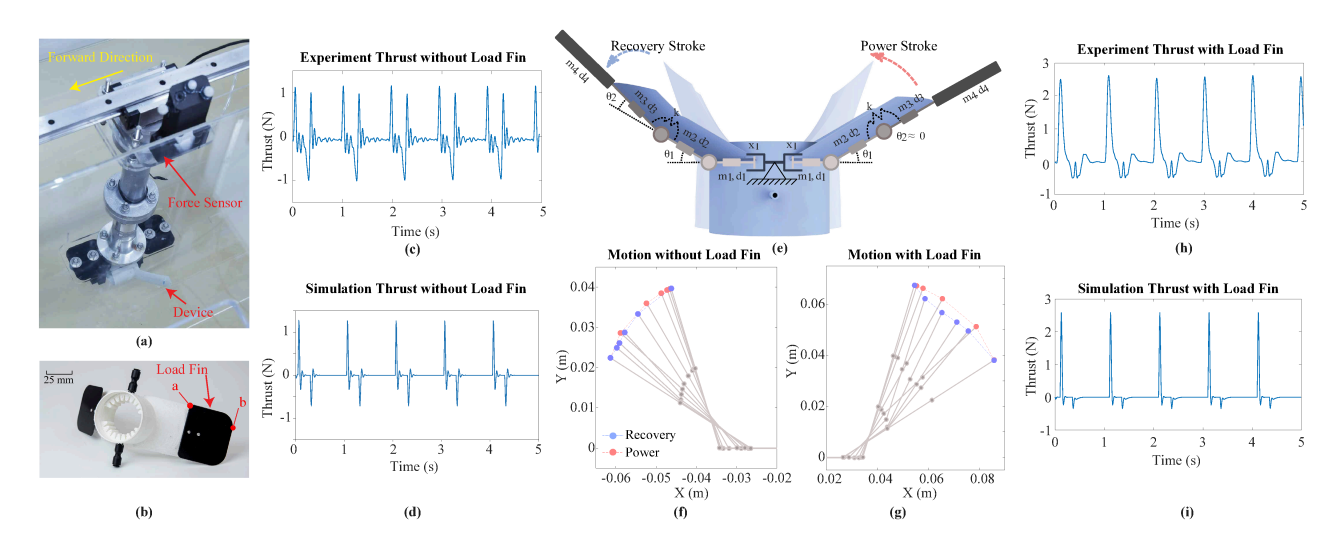


Fig. 6. Swim Test (a): The thrust test setup. (b): The device with the load fin. (c): The thrust measured without load fin at frequency = 1 Hz. (d): The thrust measured with load fin at frequency = 1 Hz. (e): The proposed dynamic model. (f): The simulation trajectory of the paddling gait with load fin. (g): The simulation trajectory of the paddling gait without load fin. (h): The simulation thrust without load fin. (i): The simulation thrust with load fin.

forward thrust is measured using the prototype in Fig. 5d. The device is attached to a force sensor and then fixed in the water, as shown in Fig. 6a. During the test, the air pressure is regulated to 60 psi to make sure that the tube can be fully deformed. A 2-position solenoid valve (NITRA, AVS-3212-24D) is selected to control the air inflation and deflation. The air inflation and deflation cycle is commanded at different frequencies while the thrust generated by the device is recorded. After running multiple sets of tests at different frequencies, the highest thrust was obtained at the solenoid's maximum cycle speed of 1 Hz. The thrust over time for this case is shown in Fig. 6c. This plot shows that the positive forward thrust produced by the fin during the power stroke reaches 1.2N, while the minimum thrust value, obtained during the recovery stroke reaches -0.98N; the net thrust averaged over a full cycle is -0.05N. Because of low drag and inertial loads acting on the fin, buckling in the fins was not readily observed during the test. When allowed to swim freely, the prototype traveled a negligible distance over a large number of cycles.

In order to induce buckling and generate more asymmetric thrust, a fin extension (called the "load fin") was attached to the device, as shown in Fig. 6b. It is made of fiberglass and weighs 2.05 g. The test was then repeated at the same air pressure and frequency; the result is shown in Fig. 6d. Due to the increased drag from the load fin, the peak thrust during the power stroke increases to 2.6 N, but - due to buckling during the recovery stroke - the peak minimum thrust drops to -0.47 N. Overall net thrust, averaged over the full cycle, increases from -0.05 N to 0.23 N. This increase in net forward thrust is also reflected in better swimming results; when the system with attached load fins swam freely in the tank it reached an average forward swimming speed of 53 mm/s, which is 1.33 body length per second. This result can be seen in the supplementary video associated with the paper. Base on the Reynolds number of a flapping wing in fluid, formulated from [44], [45], the Reynolds number of the device was calculated using $Re = \frac{\bar{u}\bar{v}}{v}$, where \bar{u},\bar{c} and v are the

mean translational velocity of the wing tip, the mean chord length, and the kinematic viscosity of the fluid, respectively. In this proposed system, the mean translational velocity of the wing tip \bar{u} is analysed from the slow motion video. We measured the velocity at two locations of the fin under both power stroke and recover stroke. For the tip of the load fin, which is the point b in Fig. 6b, the translational velocity at the power stroke is $\bar{u} = 29.76 \text{ mm/s}$, the translational velocity at the recover stroke is $\bar{u} = 24.2 \text{ mm/s}$. This leads to the Reynolds number within the range of 2024 to 2490. As for the tip of the TPE fin, which is the point a in Fig. 6b, $\bar{u} = 19.2 \text{ mm/s}$ at the power stroke cycle, and $\bar{u} = 16.2 \text{ mm/s}$ at the recover stroke. The Reynolds number of the system is then calculated to be vary from 855 to 1014. This indicates that the system flow regime changes from laminar to turbulent.

C. Dynamic Modeling

In this section, we describe the dynamic modeling of the system, focusing on the curved fins' asymmetric buckling behavior and its effect on thrust generation; studying the system's dynamic behavior under similar conditions with the experimental swimming thrust tests covered in Sec. V. In the proposed dynamic model (Fig. 6e, each half of the system is represented by three planar rigid links (x_1 , m_1 , and d_2 , m_2 , and d_3 , m_3) with point masses located at the links' midpoints. Tube deformation is modeled as a prismatic joint, while each fin is modeled by two rigid links that are connected by pin joints and a nonlinear torsional spring.

We first experimentally identify a model describing the effect of the pneumatic activation and the curvature propagation on the attachment (x_1) and its rotation (θ_1) . These parameters are measured using the experimental setup in Fig 5e, across input pressures ranging from 0-40 psi. The fins' rotation about the tube is modeled as a function of x_1 , which is derived from experimental measurements. In our dynamic model, we use a combination of a horizontal input force and a spring-damper mechanism in order to match the

variation of x_1 in time to best fit the experimentally-collected motion of the fins' proximal connection.

Using the above relations, the pneumatic actuation, tube deformation, and fin configuration can be modeled under no-load conditions. The distal portion of the fin's asymmetric deformation and stiffness under load (K) are next modeled. Using the nonlinear behavior of the curved fins (Figs. 5a, b) and the fins' configuration for each tube deformation, the fins' equal and opposite-sense bending under load are represented as a torsional spring with variable stiffness; this is a function of the tube's deformation (x), fin orientation (x), and curvature (x). A two-term exponential function is applied to fit experimentally-collected data correlating the measured stiffness (x) against all configurations.

Using a flat plate model derived from [46], the forces on the fin due to the fluid are estimated as

$$F_{w_D} = \rho u^2 A \sin^2 \alpha \tag{1}$$

$$F_{w_I} = \rho u^2 A \cos \alpha \sin \alpha, \qquad (2)$$

where ρ , u, A, and α are the density of fluid, the relative velocity of the plate, the area of the plate, and the angle of attack of the wing, respectively. F_{w_D} and F_{w_L} correspond to the drag and lift components of aerodynamic forces acting on the plate. The total force on a flat plate is estimated as

$$F_{w} = \rho u^{2} A \sin \alpha, \tag{3}$$

where α is 0 when parallel to the flow and 90° when perpendicular (in 2D) [46]. This force is perpendicular to the wing and acts as the fluid's dynamic load on the distal end of the curved beam. Based on previous work, we have shown that the error between a flat plate model and a Computational Fluid Dynamic model is less than 15% for a device at a similar scale and speed, with a maximum Reynolds number less than 7200 [36]. When the system is within the laminar regime, the flat plate model has a high correlation with the CFD result. Thus, we believe that the flat plate approximation holds well in this case as well, especially since it reduces computational complexity and simulation time.

The dynamic model is then evaluated by comparing the model's thrust estimate against data collected experimentally. By defining rigid constraints connecting the main body of the robot to ground, the forces exerted on the environment when a fin is actuated can thus be measured. Two cases are considered: the thrust generated by the fins alone (Fig. 5h), and with the extra load fins attached (Fig. 5i). Similar to the experiment, the results show that the positive net thrust is generated due to the asymmetric stiffness model identified for k (Fig. 6h), however, buckling is not obvious in the first case due to the smaller inertias and lower drag acting on the fins (Fig. 6g). The maximum and minimum thrust estimated by the model for this case are 1.2 N and -0.72 N, respectively. Fig. 6f,h show the model's estimate of a fin's motion and thrust generated across multiple cycles in the second case, respectively. These data reveal that the contribution of inertia and drag from the load fin increases the loading on the beam, forcing it to undergo buckling. This results in a minimum

thrust of -0.38 N during recovery, smaller than case 1. By contrast, the maximum positive thrust increases to 2.58 N.

Comparing the simulation and experimental results show that the proposed dynamic model is capable of estimating the system behavior for both cases and can effectively implement the nonlinear behavior of the curved fins. We believe this model will inform future design optimization aiming to increase the efficacy of the proposed mechanism.

VI. CONCLUSIONS AND FUTURE WORK

This paper summarizes our current work in understanding how to leverage curvature change, shape propagation, buckling, and hysteresis in soft systems to reduce the actuation and control complexity for swimming. Through the use of the dynamic models presented herein, we have demonstrated the potential for further improving performance in Soft, Curved, Reconfigurable Anisotropic Mechanisms, or SCRAMs by showing how small changes in loading conditions can induce larger changes in thrust and work generation. Finally, by creating a monolithic, 3D-printed prototype, we have demonstrated how future designs may be printed on demand as the result of a more integrated optimization pipeline.

Future work will focus on untethered, autonomous swimming applications in which multiple fins are attached to a single power source; we seek to apply the concept of pneumatically pinched tubes to further increase the available degrees of freedom in such systems and reconfigure such robots for multi-modal locomotion in a variety of media. This will require much tighter integration of simulation and modeling to include fluid or granular interactions as well as more optimized design geometries to obtain more energy efficient locomotion. Furthermore, we need to enhance the versatility of fluid dynamics modelling to cover both laminar and turbulent regimes; this will enable us to model system behavior at various scales and actuation speeds.

VII. APPENDIX

 $\begin{tabular}{ll} TABLE\ I \\ PARAMETERS\ IN\ FINAL\ PROTOTYPE \\ \end{tabular}$

Variable	Parameter	Variable	Parameter
D (mm)	50	L(mm)	50
α (degree)	65	θ (degree)	60
w (mm)	5	h (mm)	5
<i>t</i> ₁ (mm)	0.4	t ₂ (mm)	1.5
l (mm)	14	t_f (mm)	2
n	9		

REFERENCES

- [1] S. H. Gittelman, "Locomotion and predatory strategy in backswimmers (hemiptera: Notonectidae)," *The American Midland Naturalist*, vol. 92, no. 2, pp. 496–500, 1974. [Online]. Available: http://www.jstor.org/stable/2424316
- [2] F. Jizhuang, Z. Wei, Y. Bowen, and L. Gangfeng, "Propulsive efficiency of frog swimming with different feet and swimming patterns," *Biology Open*, vol. 6, no. 4, pp. 503–510, 2017.
- [3] J. M. Gal and R. W. Blake, "Biomechanics of Frog Swimming," Journal of Experimental Biology, vol. 138, pp. 399–411, 1988.

- [4] C. J. Clemente and C. Richards, "Muscle function and hydrodynamics limit power and speed in swimming frogs," *Nature Communications*, vol. 4, no. May, 2013.
- [5] S. ITO and A. AZUMA, "Analysis of thrust performance for paddling locomotion," *Theoretical and Applied Mechanics*, vol. 50, pp. 271– 280, 2001.
- [6] H.-J. Kim, S.-H. Song, and S.-H. Ahn, "A turtle-like swimming robot using a smart soft composite (SSC) structure," *Smart Materials and Structures*, vol. 22, no. 1, p. 014007, dec 2012. [Online]. Available: https://doi.org/10.1088%2F0964-1726%2F22%2F1%2F014007
- [7] L. Ristroph, A. J. Bergou, J. Guckenheimer, Z. J. Wang, and I. Cohen, "Paddling mode of forward flight in insects," *Physical Review Letters*, vol. 106, no. 17, pp. 1–4, 2011.
- [8] F. E. Fish, N. K. DiNenno, and J. Trail, "The "dog paddle": Stereotypic swimming gait pattern in different dog breeds," *Anatomical Record*, no. January, pp. 1–11, 2020.
- [9] H. Takagi, S. Sugimoto, N. Nishijima, and B. Wilson, "Swimming: Differences in stroke phases, arm-leg coordination and velocity fluctuation due to event, gender and performance level in breaststroke," *Sports Biomechanics*, vol. 3, no. 1, pp. 15–27, 2004.
- [10] F. Dadashi, A. Arami, F. Crettenand, G. P. Millet, J. Komar, L. Seifert, and K. Aminian, "A hidden Markov model of the breaststroke swimming temporal phases using wearable inertial measurement units," 2013 IEEE International Conference on Body Sensor Networks, BSN 2013, pp. 1–6, 2013.
- [11] I. Holmér, "Propulsive efficiency of breaststroke and freestyle swimming," European Journal of Applied Physiology and Occupational Physiology, vol. 33, no. 2, pp. 95–103, 1974.
- [12] K. G. Thompson, D. P. MacLaren, A. Lees, and G. Atkinson, "The effects of changing pace on metabolism and stroke characteristics during high-speed breaststroke swimming," *Journal of Sports Sciences*, vol. 22, no. 2, pp. 149–157, 2004.
- [13] C. López and J. Serna, "Quantitative analysis of kayak paddling technique: Definition of an optimal stroke profile," *Revista Andaluza* de Medicina del Deporte, vol. 4, pp. 91–95, 01 2011.
- [14] Y. Sun, S. Ma, K. Fujita, Y. Yang, and H. Pu, "Modeling the rotational paddling of an ePaddle-based amphibious robot," *IEEE International Conference on Intelligent Robots and Systems*, pp. 610–615, 2012.
- [15] F. Jizhuang, D. Qilong, Y. Qingguo, W. Yi, Q. Jiaming, and Z. Yanhe, "Biologically inspired swimming robotic frog based on pneumatic soft actuators," *Bioinspiration and Biomimetics*, vol. 15, no. 4, 2020.
- [16] Y. Li, F. Fish, Y. Chen, T. Ren, and J. Zhou, "Bio-inspired robotic dog paddling: Kinematic and hydro-dynamic analysis," *Bioinspiration* and *Biomimetics*, vol. 14, no. 6, 2019.
- [17] H. Park, S. Park, E. Yoon, B. Kim, J. Park, and S. Park, "Paddling based microrobot for capsule endoscopes," *Proceedings - IEEE International Conference on Robotics and Automation*, no. April, pp. 3377–3382, 2007.
- [18] H. Pu, Y. Sun, Y. Yang, S. Ma, and Z. Gong, "Modeling of the oscillating-paddling gait for an ePaddle locomotion mechanism," Proceedings - IEEE International Conference on Robotics and Automation, pp. 3429–3435, 2013.
- [19] Q. Pan and S. Guo, "A paddling type of microrobot in pipe," Proceedings - IEEE International Conference on Robotics and Automation, pp. 2995–3000, 2009.
- [20] M. P. Ford, H. K. Lai, M. Samaee, and A. Santhanakrishnan, "Hydrodynamics of metachronal paddling: Effects of varying Reynolds number and phase lag," *Royal Society Open Science*, vol. 6, no. 10, 2019.
- [21] D. A. Huffman, "Curvature and Creases: A Primer on Paper," IEEE Transactions on Computers, vol. C-25, no. 10, pp. 1010–1019, 1976.
- [22] J. P. Duncan and J. L. Duncan, "Folded developables," Proceedings of the Royal Society of London. A. Mathematical and Physical Sciences, vol. 383, no. 1784, pp. 191–205, 1982.
- [23] Y. L. Kergosien, H. Gotoda, and T. L. Kunii, "Bending and Creasing Virtual Paper," *IEEE Computer Graphics and Applications*, vol. 14, no. 1, pp. 40–48, 1994.
- [24] S. Miyashita, I. DiDio, I. Ananthabhotla, B. An, C. Sung, S. Arabagi, and D. Rus, "Folding angle regulation by curved crease design for self-assembling origami propellers," *Journal of Mechanisms and Robotics*, vol. 7, no. 2, pp. 1–8, 2015.
- [25] J. M. Gattas, "Miura-Base Rigid Origami: Parametrizations of Curved-Crease Geometries," vol. 136, no. December 2014, pp. 1–10, 2016.

- [26] E. D. Demaine and M. L. Demaine, "Curved Crease Folding a Review on Art, Design and Mathematics Curved Creases in Art and Design."
- [27] T. Tachi and G. Epps, "Designing One-DOF Mechanisms for Architecture by Rationalizing Curved Folding," Proceedings of the International Symposium on Algorithmic Design for Architecture and Urban Design, no. October, 2011.
- [28] S. Miyashita, S. Guitron, M. Ludersdorfer, C. R. Sung, and D. Rus, "An untethered miniature origami robot that self-folds, walks, swims, and degrades," *Proceedings - IEEE International Conference on Robotics and Automation*, vol. 2015-June, no. June, pp. 1490–1496, 2015.
- [29] V. Pini, J. J. Ruz, P. M. Kosaka, O. Malvar, M. Calleja, and J. Tamayo, "How two-dimensional bending can extraordinarily stiffen thin sheets," *Scientific Reports*, vol. 6, no. July, pp. 1–6, 2016.
- [30] Y. Jiang, M. Sharifzadeh, and D. M. Aukes, "Reconfigurable soft flexure hinges via pinched tubes (accepted)," *IEEE International Conference on Intelligent Robots and Systems*, 2020. [Online]. Available: https://idealab.asu.edu/assets/jiang-iros-2020.pdf
- [31] N. P. Bende, A. A. Evans, S. Innes-Gold, L. A. Marin, I. Cohen, R. C. Hayward, and C. D. Santangelo, "Geometrically controlled snapping transitions in shells with curved creases," *Proceedings of the National Academy of Sciences of the United States of America*, vol. 112, no. 36, pp. 11175–11180, 2015.
- [32] R. Vogel and H. Stark, "Motor-driven bacterial flagella and buckling instabilities," *The European Physical Journal E*, vol. 35, no. 2, p. 15, 2012.
- [33] A. G. Volkov, T. Adesina, V. S. Markin, and E. Jovanov, "Kinetics and mechanism of dionaea muscipula trap closing," *Plant physiology*, vol. 146, no. 2, pp. 694–702, 2008.
- [34] V. S. Markin, A. G. Volkov, and E. Jovanov, "Active movements in plants: mechanism of trap closure by dionaea muscipula ellis," *Plant signaling & behavior*, vol. 3, no. 10, pp. 778–783, 2008.
- [35] K. Saito, S. Nomura, S. Yamamoto, R. Niiyama, and Y. Okabe, "Investigation of hindwing folding in ladybird beetles by artificial elytron transplantation and microcomputed tomography," *Proceedings* of the National Academy of Sciences, vol. 114, no. 22, pp. 5624–5628, 2017.
- [36] M. Sharifzadeh and D. Aukes, "Curvature-induced buckling for flapping-wing vehicles," *IEEE/ASME Transactions on Mechatronics*, pp. 1–1, 2020.
- [37] F. Ilievski, A. D. Mazzeo, R. F. Shepherd, X. Chen, and G. M. Whitesides, "Soft Robotics for Chemists," *Angewandte Chemie*, vol. 123, no. 8, pp. 1930–1935, 2011.
- [38] B. Gorissen, D. Reynaerts, S. Konishi, K. Yoshida, J. W. Kim, and M. De Volder, "Elastic Inflatable Actuators for Soft Robotic Applications," *Advanced Materials*, vol. 29, no. 43, pp. 1–14, 2017.
- [39] H. K. Yap, H. Y. Ng, and C. H. Yeow, "High-Force Soft Printable Pneumatics for Soft Robotic Applications," *Soft Robotics*, vol. 3, no. 3, pp. 144–158, 2016.
- [40] B. Mosadegh, P. Polygerinos, C. Keplinger, S. Wennstedt, R. F. Shepherd, U. Gupta, J. Shim, K. Bertoldi, C. J. Walsh, and G. M. Whitesides, "Pneumatic networks for soft robotics that actuate rapidly," Advanced Functional Materials, vol. 24, no. 15, pp. 2163–2170, 2014.
- [41] B. N. Peele, T. J. Wallin, H. Zhao, and R. F. Shepherd, "3D printing antagonistic systems of artificial muscle using projection stereolithography," *Bioinspiration and Biomimetics*, vol. 10, no. 5, p. 55003, 2015. [Online]. Available: http://dx.doi.org/10.1088/1748-3190/10/5/055003
- [42] UltiMaker, "Technical data sheet: TPU 95A," 2018, version 4.002. [Online]. Available: https://support.ultimaker.com/hc/en-us/ article_attachments/360010206979/TDS_TPU_95A_EN.pdf
- [43] 3DXFlex, "Technical data sheet: 3DXFLEXTM TPE 3D Printing Filament made using PEBAX[®] elastomer." [Online]. Available: https://www.3dxtech.com/content/Flex_PEBAX_TPE_v1.pdf
- [44] J. P. Whitney, "Design and performance of insect-scale flapping-wing vehicles," Ph.D. dissertation, 2012.
- [45] K. Mazaheri and A. Ebrahimi, "Experimental investigation of the effect of chordwise flexibility on the aerodynamics of flapping wings in hovering flight," *Journal of Fluids and Structures*, vol. 26, no. 4, pp. 544–558, 2010.
- [46] J. W. Roberts, R. Cory, and R. Tedrake, "On the controllability of fixed-wing perching," in *Proceedings of the American Control Conference*, no. 1. IEEE, 2009, pp. 2018–2023. [Online]. Available: http://ieeexplore.ieee.org/document/5160526/